Title	A strain-gradient, crystal plasticity model for microstructure-sensitive fretting crack initiation in ferritic-pearlitic steel for flexible marine risers
Author(s)	Ashton, Patrick; Harte, Annette M.; Leen, Sean B.
Publication Date	2018-02-03
Publication Information	Ashton, P. J., Harte, A. M., & Leen, S. B. (2018). A strain-gradient, crystal plasticity model for microstructure-sensitive fretting crack initiation in ferritic-pearlitic steel for flexible marine risers. International Journal of Fatigue, 111, 81-92. doi: https://doi.org/10.1016/j.ijfatigue.2018.01.028
Publisher	Elsevier
Link to publisher's version	https://doi.org/10.1016/j.ijfatigue.2018.01.028
Item record	http://hdl.handle.net/10379/15594
DOI	http://dx.doi.org/10.1016/j.ijfatigue.2018.01.028

A strain-gradient, crystal plasticity model for microstructure-sensitive fretting crack initiation in ferritic-pearlitic steel for flexible marine risers

P. J. Ashton [a], A.M. Harte [b,c], S. B. Leen [a,c]

[a] Mechanical Engineering, College of Engineering and Informatics, NUI Galway, Ireland

[b] Civil Engineering, College of Engineering and Informatics, NUI Galway, Ireland

[c] Ryan Institute for Environmental, Marine and Energy Research, NUI Galway, Ireland

Abstract

A three-dimensional, strain-gradient, crystal plasticity methodology is presented for prediction of microstructure-sensitive length-scale effects in crack initiation, under fatigue and fretting fatigue conditions, for a ferritic-pearlitic steel used in flexible marine risers. The methodology, comprising length-scale dependent constitutive model and scale-consistent fatigue indicator parameters, is calibrated and validated for representative (measured) dual-phase microstructures under strain-controlled low cycle fatigue conditions. Prediction of the effects of length-scale on fretting crack initiation is based on a three-dimensional, crystal plasticity, frictional contact model to predict fretting crack location and initial growth path, accounting for the effects of crystallographic orientation. The length-scale dependent fatigue and fretting simulations predict (i) significant beneficial effect of reducing length-scale for low cycle fatigue life, (ii) complex cyclically- and spatially-varying effects and differences due to changing contact and grain length-scales, and (ii) that fretting damage generally decreases with decreasing (contact-grain) length-scale.

1.0 Introduction

Fretting damage occurs when a small-scale (typically micro-scale) cyclic relative displacement exists between two surfaces in contact. Fretting is a concern for engineering designers as localised regions of high stresses and strains in the contact act as ideal locations for fatigue cracks to nucleate, and potentially grow under a bulk load, depending on the fretting regime. The combination of relative displacement, coefficient of friction (COF) and normal load determines the fretting regime, which can be classified as gross slip, partial slip, and mixed slip regimes. Gross slip causes significant wear and material removal, and is generally considered the least detrimental fretting regime, since nucleated cracks are either 'ground away' during the wear process or propagation rates diminish due to wear-induced contact evolution and stress redistribution [1],[2].The partial slip regime causes a stick zone with slip zones near the edges of contact, where the shear traction is large enough to overcome the resisting frictional force, as shown in Figure 1. This fretting regime is of most concern in the context of fatigue due to the absence of significant wear. Fretting fatigue failure can typically be divided into three stages; crack nucleation, short crack growth within the fretting contact region and long crack growth through the component in the presence of a bulk load. The mechanisms which drive the fretting-dominated crack initiation and short crack propagation are not fully understood and are therefore the focus of this work. In particular, the role of microstructure in fretting crack initiation has not yet been fully quantified. The key aim of this paper is to develop a micromechanical finite element modelling framework to study the mechanisms which drive fretting fatigue failure.

Finite element modelling is commonly used to predict crack initiation in fretting fatigue, where stress and strain based parameters such as Fatemi-Socie (FS) [3], Smith-Watson-Topper (SWT) [4] and Ruiz [5] parameters are employed to indicate crack location. For example, Araujo and Nowell [6] compared theoretical results with experimentally observed fretting fatigue cracks. The FS and SWT

parameters both predicted cracks to initiate at the edge of contact, which was in contrast to experiments, where cracks were also observed to occur within the slip zones. Similarly, the Ruiz [5] parameter predicts cracks near the edge of contact where a sharp peak in tangential stress occurs. Indeed, the majority of commonly used continuum mechanics based parameters for fretting crack initiation predict cracks at this same location.

Lamacq et al. [7] used a simple dislocation model to identify two mechanisms of crack initiation: (i) brittle tensile fracture due to high traction stresses, where cracks initially grow approximately normal to the surface, and (ii) a slip mechanism, where cracks nucleate at surface intrusions and extrusions due to the formation of crystallographic slip bands and initially grow at a shallow angle, along the plane of maximum shear stress.

A key limitation of previous computational work on crack initiation prediction is the omission of microstructural effects, which is discussed in a number of publications [7],[8],[9]. It is well known that at the small length-scales associated with fretting fatigue, metals are not homogeneous, and consequently are not accurately represented by isotropic elastic material models, even in macroscopically elastic strain fields. Typically the highly localised contact region contains only a small number of metallic grains with varying crystallographic orientations (Fig. 1), and localised plasticity and crystallographic slip is likely to occur, even in nominally elastic loading conditions. It is therefore important to consider microstructure in fretting models to achieve a more accurate representation of the material, and hence, better understand the mechanisms that drive crack initiation.
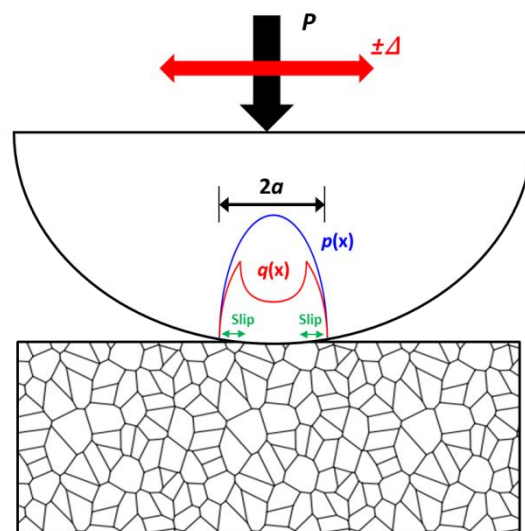

Figure 1. Schematic of cylinder-on flat fretting model showing material microstructure and indicated slip zones where the tangential force is greater than the resisting frictional force.

Research into microstructure-sensitive fretting through crystal plasticity finite element (CPFE) modelling indicates that material microstructure plays a significant role in fretting fatigue [10],[11]. The authors [12] have previously demonstrated the significant role of ratio of contact semi-width (a) to average grain size (d), a/d. Zhang et al. [13] showed that for highly anisotropic microstructures, e.g. in titanium alloys, crystallographic texture is another important factor in fretting fatigue. In the context of predicting crack location with respect to microstructure, crystal plasticity modelling is an important technique as it can represent the heterogeneity in microstructure, and therefore has the ability to identify critical features such as grain and phase boundary stress-strain concentrations and the formation of persistent slip bands [14].

A key novelty of the current work is inclusion of length-scale effects due to plastic strain gradients in micro-mechanical fretting modelling. Strain gradient effects [15],[16],[17] in metals are associated

with the occurrence of non-uniform plastic strain. Extra dislocations in the material are necessary to accommodate lattice curvature resulting from such plastic strain gradients. These dislocations, termed geometrically necessary dislocations (GNDs), are sessile in nature and act as obstacles to mobile dislocations (e.g. statistically stored dislocations [15]), resulting in localised slip system hardening.

The formation of GNDs can be explained by considering a beam in bending, as shown schematically in Fig. 2. A gradient in plastic strain exists between the centroidal axis and the surface of the bent beam, resulting in curvature of the crystal lattice. Additional dislocations are then necessary to accommodate this curvature. These effects are also seen in materials with small average grain sizes, inclusions and dual phase microstructures, where the small intrinsic length-scales result in high plastic strain gradients [18],[19]. As the characteristic length (e.g. grain size) is reduced, higher gradients of plastic strain arise, resulting in a harder material response. Although most work on this topic focuses on monotonic loading, it has been shown both experimentally and theoretically [20],[21] that the presence of GNDs also leads to a Bauschinger effect upon reverse loading.
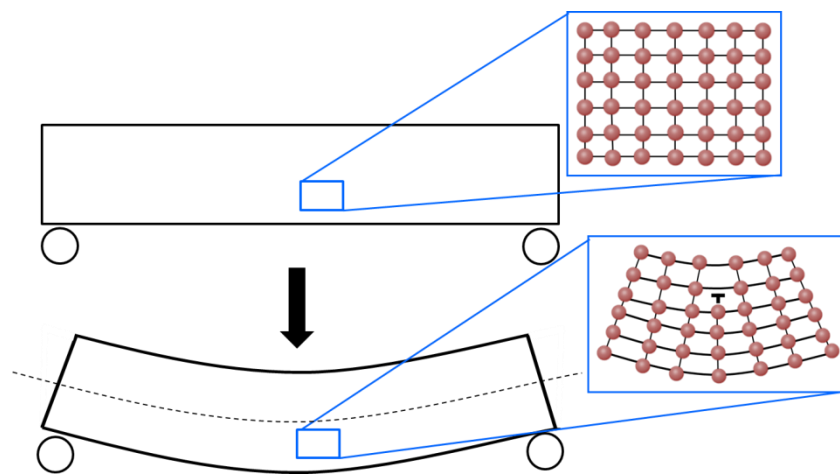

Figure 2. Schematic of GNDs arising in beam bending, where a gradient of plastic strain exists.

GNDs are potentially important in the context of fretting due to the steep stress gradients which arise at the edge of contact and the small length-scales generally associated with contact width. Indeed, a contact size effect has been observed in fretting fatigue experiments by a number of authors [22],[6],[23], where fretting fatigue life was shown to increase as the contact width decreased, as shown schematically in Fig. 3. Although previous work by the authors [12] has shown that statistical microstructural effects (e.g. due to number of grains in the contact zone) are a key contributory factor for this phenomenon, the significance of strain gradient effects in fretting has not yet been assessed.
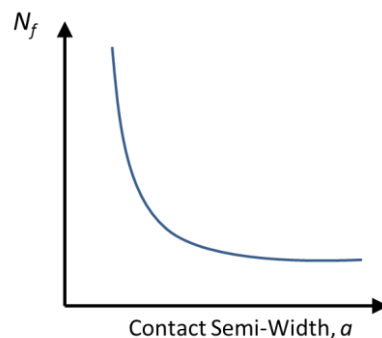

Figure 3. Schematic of contact size effects in fretting fatigue.

In this work, the microstructure of a ferritic-pearlitic steel is characterised to facilitate the generation of representative finite element microstructure geometries. Crystal plasticity material parameters are identified by calibrating a unit cell microstructure model against measured experimental data. Two micro-scale fatigue indicator parameters are implemented to predict number of cycles to crack initiation and validated against low cycle fatigue test data. A microstructure sensitive fretting model is developed to study crack initiation in fretting, with particular focus on length-scale effects. The predicted location and initial growth path of fretting cracks is investigated and compared to available experimental data and commonly used continuum based approaches. The role of length-scale effects due to plastic strain-gradients is assessed by comparing the fatigue performance of two fretting models with different characteristic lengths, but with otherwise nominally-identical mechanical and material characteristics, viz. same fretting stress distributions and same a/d ratios.

2 Material Characterisation

2.1 Characterisation of Material Microstructure

The material employed for this study is a ferritic-pearlitic steel used to manufacture the pressure armour layer of flexible marine risers, which are susceptible to fretting in service [24]. The as-received pressure armour steel material is in the form of 21 mm diameter rods. Energy-dispersive X-ray (EDX) analysis has established a carbon content of 0.4%. The microstructure of the material is composed of ferrite and pearlite phases. The pearlite phase consists of a thin lamellar structure of hard cementite and soft ferrite. Microscopy specimens were manufactured from the as-received material, mounted in epoxy resin and prepared for analysis using standard grinding, polishing and etching techniques. Optical microscopy and scanning electron microscopy (SEM) were performed to determine phase volume fraction and grain size statistics of the material. SEM images of the material microstructure are shown in Fig. 4, where the two distinct phases of ferrite (dark phase) and pearlite (light phase) phases can be seen. Figure 4b in particular, clearly shows the cementite (light) lamellae embedded in ferrite to collectively form pearlite. A Python scripting methodology has been developed here to determine microstructure statistics by implementing gaussian filter and thresholding techniques. The microstructural analysis has identified a volume fraction of 51% ferrite and 49% pearlite, with an average ferrite grain size of 11 μm.
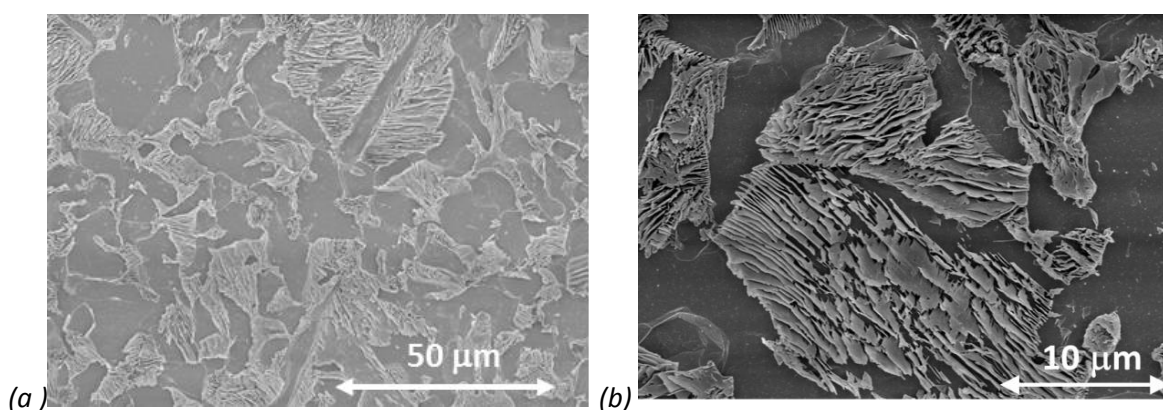

(a) (b)

Figure 4. (a) SEM image of the flexible riser pressure armour material microstructure showing the light-coloured pearlite phase and darker ferrite phase and, (b) SEM image of a pearlite colony, showing the lamellar ferrite-cementite structure.

2.2 Characterisation of Mechanical and Low Cycle Fatigue Behaviour

A program of strain-controlled low cycle fatigue (LCF) tests was conducted to characterise the cyclic plasticity and fatigue behaviour of the material and to facilitate calibration of the CPFE and fatigue prediction model. Specimens were manufactured according to the American Society for Testing and Materials (ASTM) standards and tested using an Instron 8500 servo hydraulic system. An extensometer with knife-edge probes was used to measure, and hence control, the applied strain range, using a constant rate of 0.1% per second. The fatigue specimen geometry is given in Fig. 5.

Figure 6 shows the evolution of stress range for applied strain ranges of 0.8%, 1.0%, 1.6% and 2.0%. For all but the highest strain range case, the material is seen to cyclically soften during the first 20 cycles. Gradual hardening is thereafter observed over a large fraction of the life in each test before a dramatic drop in stress range just prior to failure. Subramanya et al. [25] observed a similar stress evolution during LCF tests of a ferritic-pearlitic steel, particularly at lower strain ranges. The slight hardening observed for the highest applied strain range has also been observed by Sankaran et al. [26] and is attributed to the formation of sub-grains and dislocation accumulation at grain and phase boundaries, as a result of high plastic strains.

Figure 7 shows the cyclic stress-strain response of the material at half-life (essentially stabilised) for each strain range considered. A significant amount of kinematic hardening can be seen in each case. For example, reverse yield occurs in tension for the applied strain range of ±1%. The number of cycles to failure is plotted in Fig. 8 for two (repeat) tests at each strain range. Fatigue scatter is seen to be more significant at the lower strain ranges; this is potentially due to the absence of bulk plasticity and greater dependency of crack initiation on microstructure [27]. This data is employed for calibration of a CPFE-based material model and fatigue indicator parameters for prediction of fatigue crack initiation.
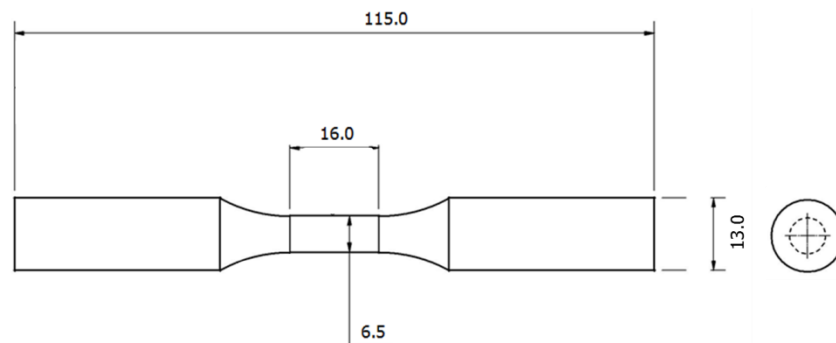

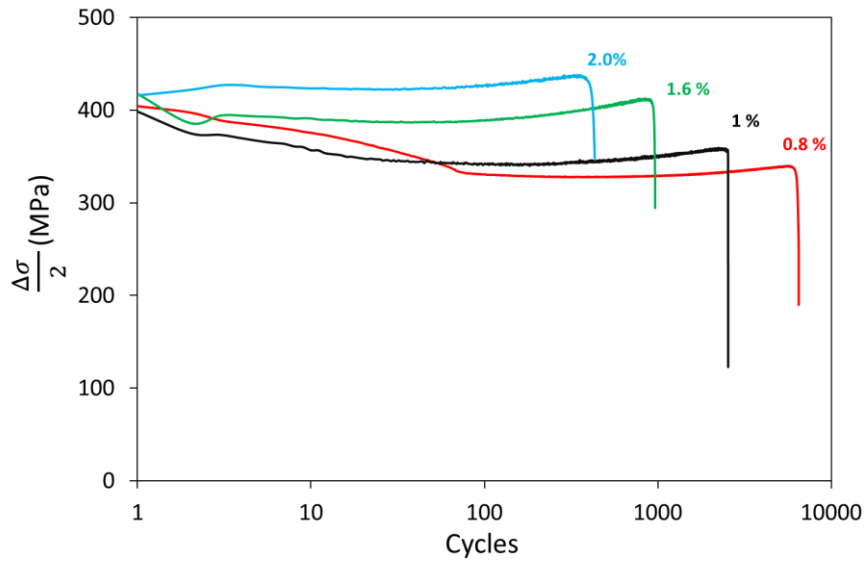*Figure 5. Fatigue specimen geometry for LCF testing (Dimensions in mm).*

Figure 6. Experimentally-measured evolutions of stress range during strain-controlled LCF tests for different strain ranges.
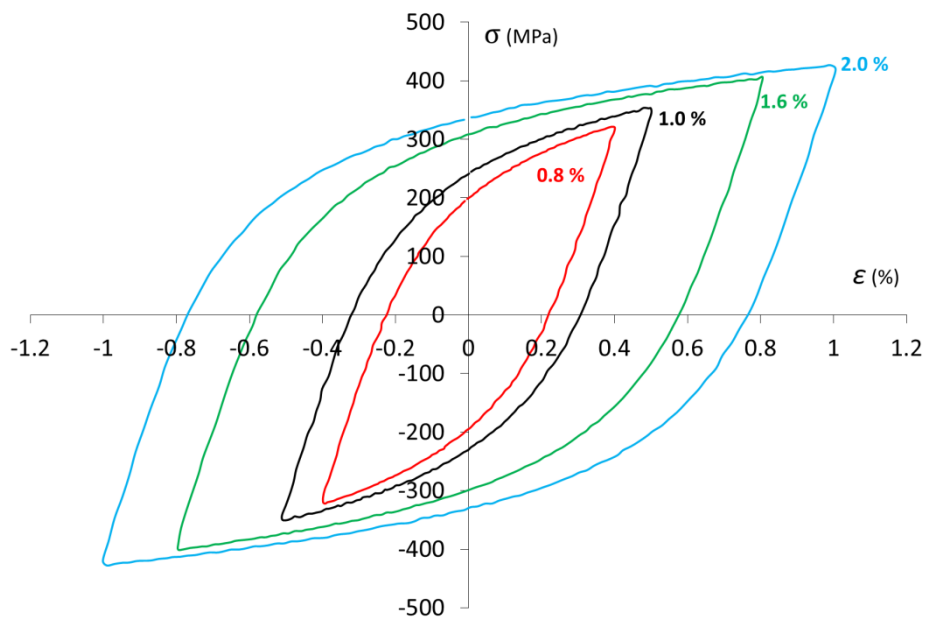

Figure 7. Experimentally-measured (half-life) cyclic stress-strain response for strain-controlled LCF tests at different strain ranges.
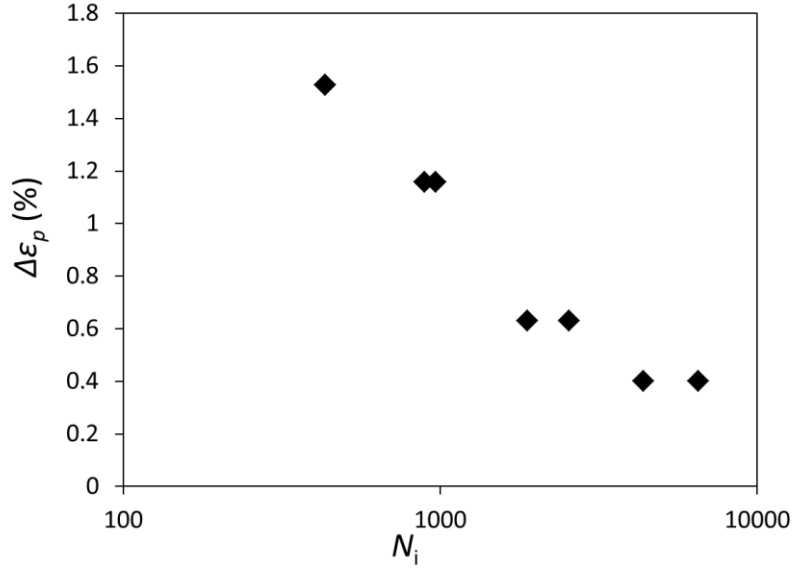
Figure 8. Experimentally-measured relationship between plastic strain range and numbers of cycles to failure, with repeat tests at each applied strain range.

3 Modelling Methodology and Calibration

3.1 Modelling approach

A CPFE modelling methodology is developed to simulate the micromechanical behaviour of the material. A unit cell microstructure model is calibrated against the experimentally measured cyclic mechanical response of the material to identify constitutive and failure parameters for the CP model. Two fatigue indicator parameters are employed to predict the number of cycles to crack initiation. Finally, a microstructure sensitive fretting model is developed to incorporate the calibrated constitutive model and realistic microstructure geometry in the contact zone and facilitate investigation of length-scale effects in fretting.

3.2 Description of model

A modified version of the crystal plasticity formulation of Dunne et al. [28] is implemented in this work. A brief description of the constitutive model is given here. Readers are referred to Ref [29] for a more detailed explanation of the original computational implementation. One of the modifications of the present implementation is the inclusion of Armstrong-Frederick type kinematic hardening to describe the significant back-stress observed in experimental tests.

The slip rule which relates slip rate to shear stress is based on the strain rate equation by Gibbs [30], where gliding dislocations are controlled by pinning at obstacles (e.g. immobile dislocation and precipitates). The slip rate $\dot{\gamma}^{\alpha}$ is related to shear stress τ^{α} on a slip system α by

$$\dot{\gamma}^{\alpha} = \rho_{SSD}^{m} v b^{\alpha 2} \exp\left(\frac{\Delta H}{-kT}\right) sinh\left(\frac{(\tau^{\alpha} - x^{\alpha} - \tau_c{}^{\alpha})\gamma_0 \Delta V^{\alpha}}{kT}\right) \tag{1}$$

where $\rho_{SSD}{}^{m}$ is the density of statistically stored mobile dislocations, v is the frequency of attempts (successful or otherwise) by dislocations to jump the energy barrier, b^{α} is Burgers vector, ΔH is Helmoltz free energy, k is the Boltzman constant, T is temperature, $\tau_c{}^{\alpha}$ is the critical resolved shear

7

stress on a particular slip system, x^{α} is a back-stress on the slip system, and γ_0 is a reference slip. The activation volume ΔV on a slip system α is defined by

$$\Delta V^{\alpha} = lb^{\alpha 2} \tag{2}$$

where l is the pinning distance between dislocations, which is related to the density of sessile SSDs, $\rho_{SSD}{}^{s}$ as follows:

$$l = \frac{1}{\sqrt{\rho_{SSD}^{s}}} \tag{3}$$

Taylor hardening [31] is chosen to describe the evolution of critical resolved shear stress, which is dependent on dislocation density [32]:

$$\tau_c{}^{\alpha} = \tau_{c0}{}^{\alpha} + MGb^{\alpha}\sqrt{\rho_{GND} + \rho_{SSD}^{s}} \tag{4}$$

where $\tau_{c0}{}^{\alpha}$ is the initial critical resolved shear stress for a slip system α, G is material shear modulus, M is the Taylor factor and ρ_{GND} is the geometrically necessary dislocation density. ρ_{GND} on a slip system is obtained by first relating closure failure of a circuit on a plane per unit area due to the presence of dislocations, as described by Nye [33], to the gradient of plastic deformation tensor $\boldsymbol{F}^{\mathrm{p}}$:

$$\sum_{\alpha=1}^{nslip} \boldsymbol{b}^{\alpha} \otimes \boldsymbol{\rho}^{\alpha}{}_{GND} = curl(\boldsymbol{F}^{\mathrm{p}}) \tag{5}$$

where $\boldsymbol{F}^{\mathrm{p}}$ is the plastic deformation gradient tensor, which is determined by decomposing the overall deformation gradient $\boldsymbol{F}$ into elastic and plastic parts:

$$\boldsymbol{F} = \boldsymbol{F}^{\mathrm{e}} \cdot \boldsymbol{F}^{\mathrm{p}} \tag{6}$$

Dislocations can be of edge ($\boldsymbol{\rho}_{\mathrm{et}}^{\alpha}$, $\boldsymbol{\rho}_{\mathrm{en}}^{\alpha}$) or screw ($\boldsymbol{\rho}_{\mathrm{s}}^{\alpha}$) type, leading to the expression:

$$\sum_{\alpha=1}^{nslip} (\rho_{\mathrm{s}}^{\alpha}\boldsymbol{b}^{\alpha} \otimes \boldsymbol{s}^{\alpha} + \rho_{\mathrm{et}}^{\alpha}\boldsymbol{b}^{\alpha} \otimes \boldsymbol{n}^{\alpha} + \rho_{\mathrm{en}}^{\alpha}\boldsymbol{b}^{\alpha} \otimes \boldsymbol{t}^{\alpha}) = curl(\boldsymbol{F}^{\mathrm{p}}) \tag{7}$$

where $\boldsymbol{s}^{\alpha}$ is the slip direction, $\boldsymbol{n}^{\alpha}$ is slip normal, and $\boldsymbol{t}^{\alpha} = \boldsymbol{s}^{\alpha} \times \boldsymbol{n}^{\alpha}$. A matrix of dyadic products $\boldsymbol{A}$ can be constructed to give

$$\boldsymbol{A}\boldsymbol{\rho}_{GND} = curl(\boldsymbol{F}^{\mathrm{p}}). \tag{8}$$

The least squares minimization procedure described by Arsenlis and Parks [34] is implemented here to calculate $\boldsymbol{\rho}_{GND}$ on each slip system. The sum of the squares of $\boldsymbol{\rho}_{GND}$ on each slip system is used for implementation of Taylor hardening in Eq. (4). A more detailed description of the calculation of spatial gradients of $\boldsymbol{F}^{\mathrm{p}}$ and $\boldsymbol{\rho}_{GND}$ is given in refs [35] and [36], respectively.

The lamellar spacing of the pearlite phase is too small (< 1µm) to model geometrically, with regards to the finite element mesh density required. As a result, the pearlite grains are homogenised and a ratio of critical resolved shear stresses is used here to distinguish between ferrite and pearlite. Ishikawa et al [37] showed experimentally that the yield strength of pure ferrite is approximately 70% that of pure pearlite. Therefore, this ratio of 0.7 is applied to the critical resolved shear stress τ_{c0} for the two phases. Although this is a relatively simple approach for modelling the pearlite phase, the ferrite phase is of most interest here, as fatigue cracks have been shown to initiate in this softer phase under fatigue loading. For example, Kucharczyk et al. [38] conducted a series of four-point bend fatigue tests on a similar material and showed that cracks always initiate in the ferrite grains.

Armstrong-Frederick type kinematic hardening is implemented to calculate the backstress x^α on a slip system α, which is related to slip rate $\dot{\gamma}^\alpha$:

$$\dot{x}^\alpha = C\dot{\gamma}^\alpha - Dx^\alpha|\dot{\gamma}^\alpha| \tag{5}$$

where C is the initial hardening modulus and D is the rate of decay. Although some authors have successfully implemented kinematic hardening formulations with $\boldsymbol{\rho}_{GND}$ induced backstresses [39],[20], explicit modelling of the lamellar pearlite geometry is required to fully capture this effect in this work. This is presently impractical for the polycrystal models considered here.

Ferrite has a body centre cubic (BCC) lattice structure with 48 possible slip systems. In this work, only the 12 <110> slip systems are modelled since it has been shown by Franciosi et al. [40] that these are the principal slip systems in BCC iron and similar materials. This also helps to reduce computational complexity, and hence runtimes, especially with the inclusion of length-scale effects for 3D fretting.

3.3 Generation of microstructure geometries

A methodology has been developed here to generate representative unit cell microstructure finite element models using ABAQUS and the Python programming language based on the experimentally-measured microstructure statistics. The unit cell model, which consists of 56 grains, and is used for calibration of the material parameters, is shown in Fig. 9a. As stated earlier, the material contains 49% pearlite and 51% ferrite phases. This is incorporated in the FE model and illustrated in Fig. 9b. A comparison of experimentally determined and finite element grain volumes is shown in Fig. 10a. The microstructure is assumed to have no preferred crystallographic texture as the material has not undergone cold forming and microstructural analysis show relatively equiaxed grains. Therefore, each grain is assigned a random crystal orientation, as illustrated in the <110> pole figure given in Fig. 10b.
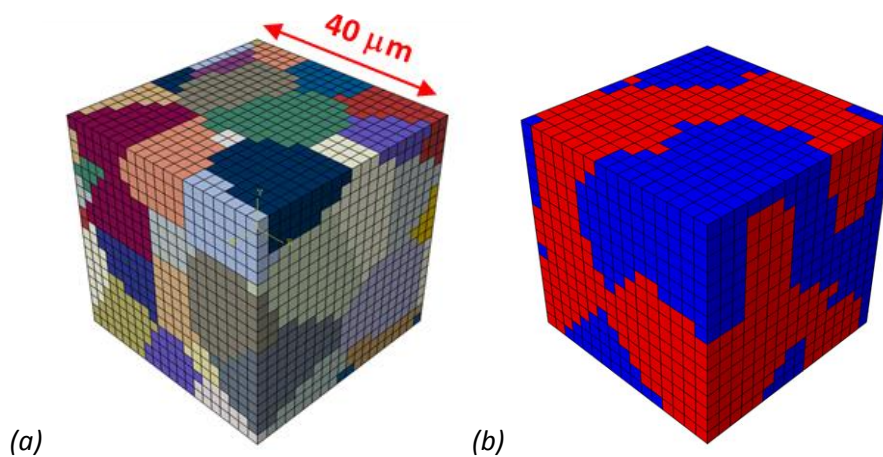

(a)   *(b)*

Figure 9. Unit cell microstructure model showing the (a) grains and (b) the ferrite (blue) and pearlite (red) phases.
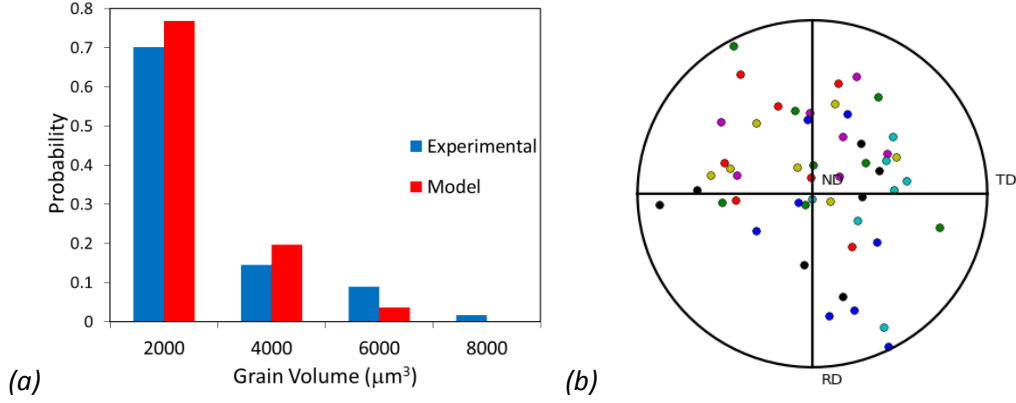
Figure 10. (a) Comparison of experimentally-determined and FE model grain volumes and (b) 110 pole figure showing randomly oriented grains.

3.4 Calibration of CP material parameters

Periodic boundary conditions are assigned to each free face of the microstructure model and a cyclic displacement is applied to simulate the microscopic deformation of a repeating unit cell in the material. A number of simulations are systematically run to calibrate the stabilised stress-strain response of the model to the experimental response, and hence, establish CPFE material parameters. The critical resolved shear stress $\tau_{c0}{}^{\alpha}$ for ferrite and the kinematic hardening parameters C and D are the only parameters calibrated here. The remaining parameters b, T, and k are established physical quantities and $\nu, \gamma_0, \rho_{SSD}$ and ΔH are adopted from previous CPFE work on ferritic steel [41]. The identified material parameters for the calibrated constitutive model are given in Table 1. A comparison of sample final CPFE stabilised hysteresis loops with the experimentally measured loops is shown in Figure 11. To ensure that the unit cell model is representative of the global response of the material, the cyclic stress strain response is compared for three different microstructure realizations (with the same average grain size and phase volume fractions) are shown in Fig. 12. It can be seen that there is no significant change in response as the microstructure is varied, and therefore, the size of the unit cell chosen is considered to be sufficiently large to represent the macroscopic deformation of the material.

Table 1. Identified parameters for CP material model.

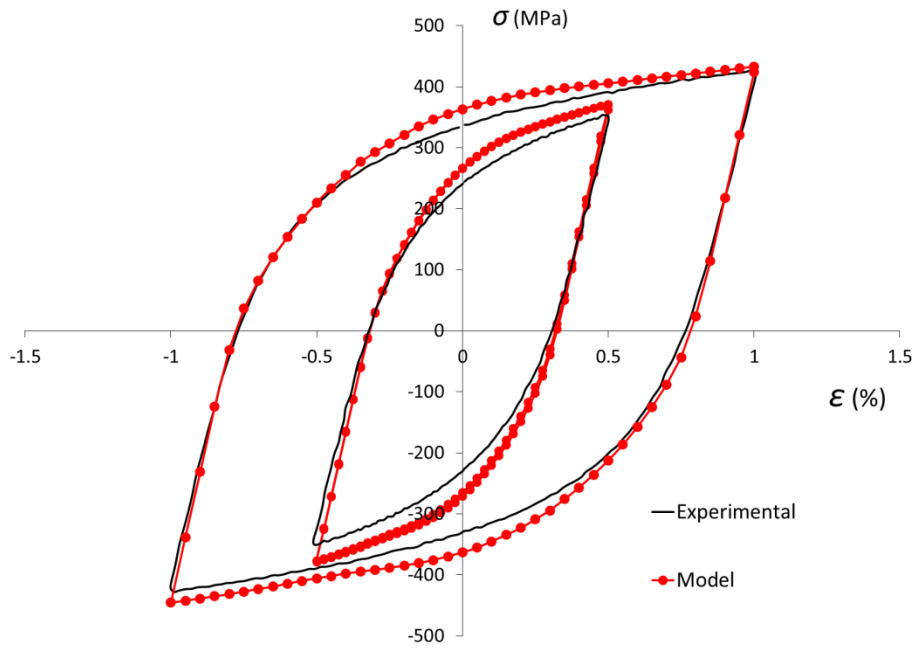| Parameter	Value
$\tau_0{}^{pearlite}$	100 MPa
$\tau_0{}^{ferrite}$	70 MPa
M	0.3
G	81.15 GPa
b	2.45 x 10^{-4} μm
k	1.38 x 10^{-23} J K^{-1}
T	293 K
ΔH	2.605 x 10^{-20} J
ν	1.00 x 10^{11} Hz
γ_0	1.0 x 10^{-3}
ρ_{SSD}	0.01 μm^{-2}
C	800 GPa
D	650

Figure 11. Comparison of experimentally measured and CPFE-predicted stabilised hysteresis loops.
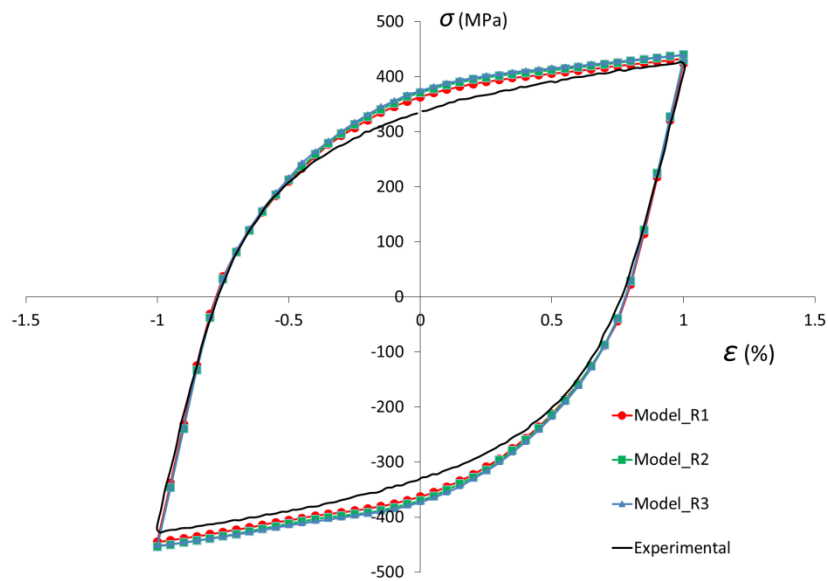

Figure 12. Comparison of CPFE-predicted unit cell response with measured (half-life) hysteresis response for three different microstructure realisations; this ensures insignificant statistical variability in response.

3.5 Strain-Gradient Length-Scale Effects

In order to demonstrate the ability of the model to capture length-scale effects due to the presence of plastic strain gradients, the cyclic stress-strain response of a 40 μm unit cell model is compared to that of a scaled-up 400 μm unit cell, as shown in Fig. 13. In this case the plastic strain gradients arise

solely from the inhomogeneity (i.e the presence of grains) in the model. The smaller 40 μm model shows a 5% larger stress range for the same applied strain resulting from relatively higher GND densities. This effect is due to the lengths over which the gradients in plastic strain exist, which are 10 times smaller in the 40 μm model, leading to more dislocations per unit volume [18], and thus, a higher GND density. Contour plots of GND density are given in Fig. 14, where the higher values can clearly be seen in the 40 μm model. The response of both models would be identical if the strain gradient formulation were omitted.
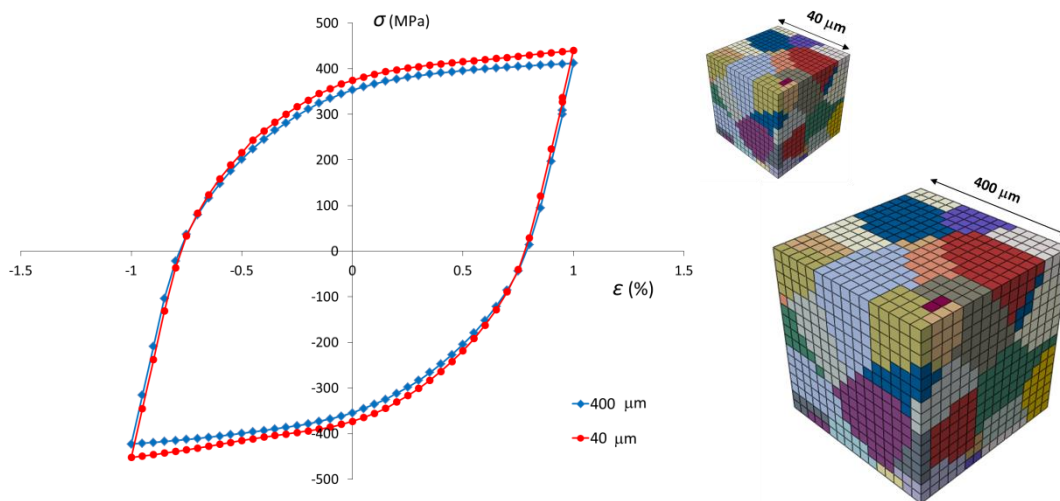

Figure 13. Comparison of cyclic stress-strain hysteresis response for 40 μm unit cell and 400 μm unit cell microstructure model, thus demonstrating the length-scale effect for plain fatigue, due to inclusion of GND hardening within the strain gradient plasticity constitutive model.
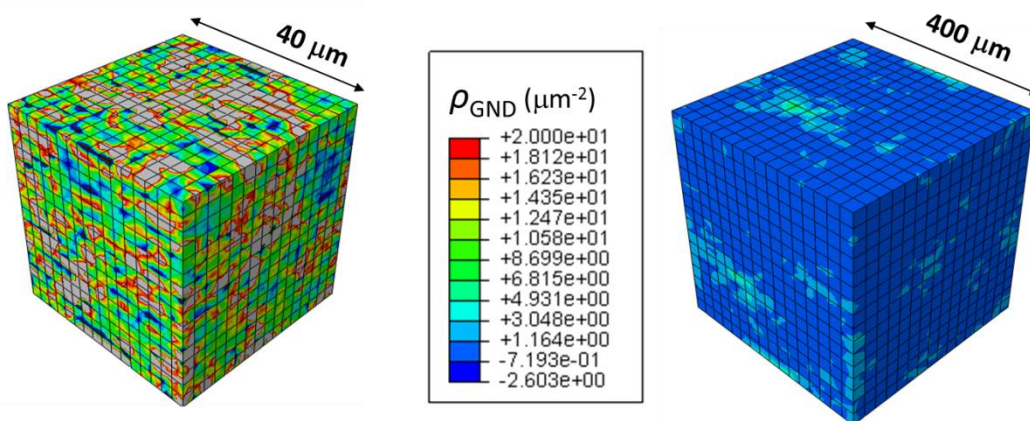

Figure 14. Contour plots of GND density for the 40 μm and 400 μm unit cell models after 3 cycles.

3.6 Prediction of fatigue crack initiation

In this work, we adopt scale-consistent fatigue indicator parameters (FIPs) for use with the crystal plasticity modelling. These parameters adopt micro-scale quantities, such as crystallographic slip, to predict crack location and number of cycles to initiation.

Two such scale-consistent FIPs are implemented here: the first, based on the work of Dunne and Manonukul [14] is the accumulated crystallographic slip parameter, designated here as p; the

second is a Fatemi-Socie (FS) [3] type parameter which is comprised of crystallographic slip and normal stress on corresponding crystallographic planes. The accumulated crystallographic slip parameter p is calculated using the rate of plastic deformation tensor $\boldsymbol{D}_\mathrm{p}$, which is obtained from the velocity gradient $\boldsymbol{L}^\mathrm{p}$:

$$\boldsymbol{L}^\mathrm{p} = \dot{\boldsymbol{F}}^\mathrm{p} \cdot \boldsymbol{F}^{\mathrm{p}-1} \tag{10}$$

$$\boldsymbol{D}^\mathrm{p} = \frac{1}{2}(\boldsymbol{L}^\mathrm{p} + (\boldsymbol{L}^\mathrm{p})^\mathrm{T}) \tag{11}$$

$$\dot{p} = (\frac{2}{3}\boldsymbol{D}^\mathrm{p}{:}\boldsymbol{D}^\mathrm{p})^{\frac{1}{2}} \tag{12}$$

$$p = \int_0^t \dot{p}\,dt \tag{13}$$

This parameter has been shown to identify persistent crystallographic slip bands [14], which are known crack initiation sites in fatigue of ferrite-pearlite steels [25] .The number of cycles to crack initiation N_i is determined by the following bi-linear Coffin Manson approach (see Cruzado et al. [42]):

$$N_i = \frac{p_\mathrm{crit}}{(p_\mathrm{cyc})^b} \tag{13}$$

where

$$p_\mathrm{cyc} = p(t) - p(t - \Delta t_{cyc}). \tag{14}$$

Δt_{cyc} is the time taken to complete one fatigue cycle, p_crit is an identified critical value, and b is an exponent.

The second FIP, based on the Fatemi-Socie macro-scale parameter [3], considers the contribution of normal stress and slip on each crystal plane, as shown schematically in Fig. 15. It has recently been implemented successfully by Sharaf et al. [43] for predicting fatigue life of ferritic–pearlitic steel in fatigue. This parameter first considers the accumulation of slip and normal stress on each non-parallel slip plane i.

$$P_{FS_i} = \int_0^t (1 + k'\frac{\sigma_n}{\sigma_y})\sum_{x=1}^N |\dot{\gamma}_i^x|\,dt \tag{15}$$

where x is the number of slip systems on a slip plane i. Here, only the 6 {110} slip planes are considered, and hence x = 2 and i = 6 (two slip systems on each plane). σ_n is the stress normal to the plane, σ_y is the macroscopic yield strength of the material, and k' is a constant which determines the contribution of normal stress to crack initiation (chosen here to be 0.5 [43]). The maximum value of P_{FS} is considered most likely to accommodate crack nucleation and therefore:

$$N_i = \frac{P_{FS\,\mathrm{crit}}}{(\max(P_{FS})_\mathrm{cyc})^b} \tag{15}$$

An advantage of this parameter is the potential to predict initial crack growth paths by identifying critical crystallographic planes on which cracks are predicted to initiate and initially propagate.
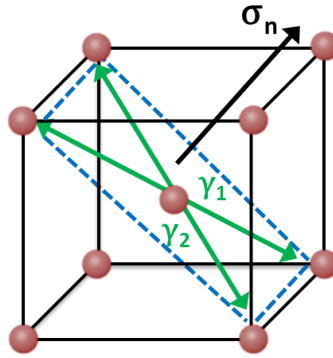
Figure 15. Schematic of BCC crystal indicating the slip and normal stress values used for the calculation of FS parameter on a crystallographic plane.

In this work, the crack initiation stage is considered to consume the majority of fatigue life, as discussed by a number of authors [14],[44]. The crack propagation stage is therefore neglected, allowing the experimentally measured LCF lives to be used for calibration of an FIP. The unit cell model described previously is employed to identify critical FIP values FIP_{crit} and exponent b based on comparison against the corresponding measured strain-range data. Calibration is carried out for a single strain range, where a cyclic strain-controlled simulation is run until the maximum value of FIP_{cyc} has stabilised. The model is then fit to the corresponding experimental data point to identify values of FIP_{crit} and b. Simulations are run for the remaining three strain ranges to validate FIP_{crit} and observe the quality of N_i prediction. A comparison of experimentally measured and CPFE-predicted N_i values is shown in Fig. 16 for each strain range. Both FIPs show general agreement with the experimental data across all strain ranges. The identified values of FIP_{crit} and b for each parameter are given in Table 2.
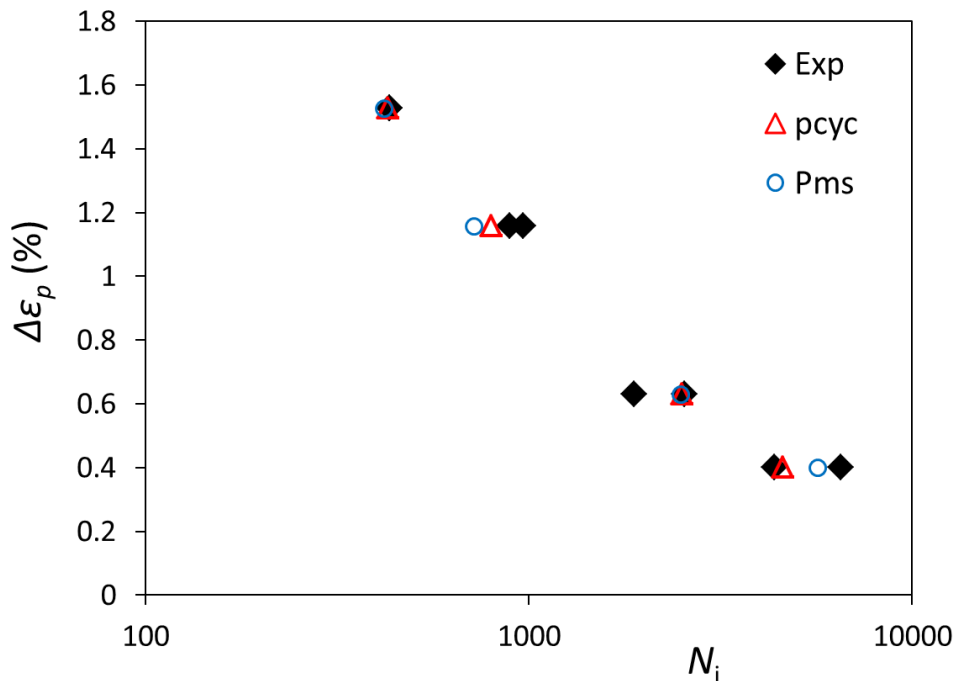

Figure 16. Comparison of CPFE predicted and experimentally observed numbers of cycles to crack initiation.

FIP	FIP$_{crit}$	b
p	6	1.8
P_{FS}	20	1.4

4 Application to Fretting

4.1 Micromechanical Fretting Model

A 3D microstructure sensitive cylinder-on-flat fretting model is developed based on previous work [12] by the authors. In order to reduce computational expense, only the contact region of the substrate is modelled using the calibrated CP constitutive model and representative ferrite-pearlite microstructure geometries. The surrounding regions are assigned a homogeneous isotropic elastic material model. Three distinct regions are created to allow for rapid mesh refinement. Tied surface constraints are utilised to connect these three separate 'parts' in the FE model, similar to the approach of Zhang et al. [13]. Coulomb friction is applied using the Lagrange multiplier technique and the assigned value appropriate to the material. The coefficient of friction of 0.6 is chosen based on the experimental fretting characterisation of O'Halloran [24], for pressure armour steel material. An applied normal load P of 16 N/mm and tangential displacement Δ of ±0.25 μm are chosen to simulate partial slip conditions. This results in a contact semi-width a of 34 μm and a peak contact pressure p_o of approximately 310 MPa. A schematic of the model is given in Fig. 17, showing loading and boundary conditions. In addition to the boundary conditions in Fig. 17, all faces parallel to the X-Y plane are constrained in the Z direction to reduce edge effects.
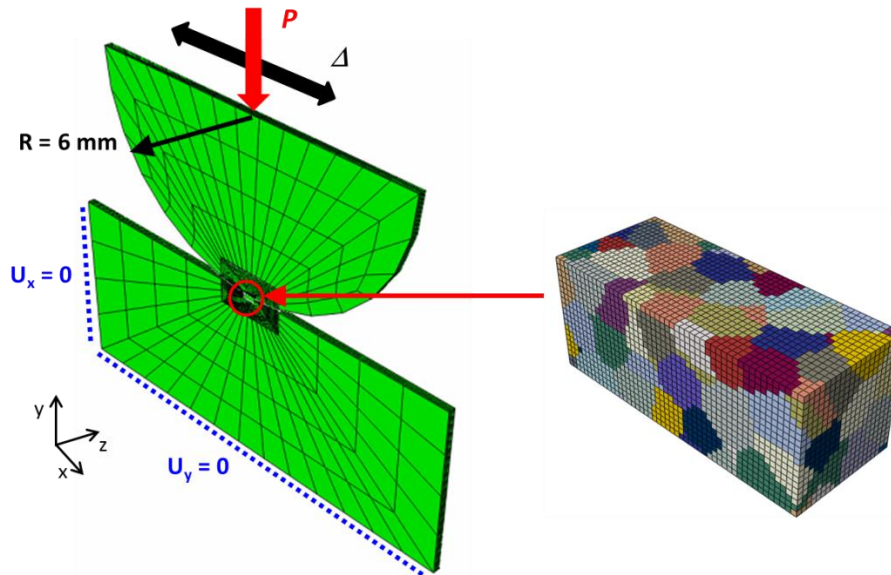

Figure 17. 3D fretting model (R = 6 mm case) showing key loading and boundary conditions and incorporation of ferritic-pearlitic steel microstructure in the contact region of the substrate.

The microstructure mesh consists of 20000 twenty-noded reduced integration elements with an average of 189 elements per grain. This is an extremely complex computational model due to the combination of three-dimensional frictional contact and strain gradient crystal plasticity constitutive model. As a result, it is not feasible to simulate a large numbers of fretting cycles. However previous CPFE fretting work [12] has shown that plastic strain distributions and cyclic accumulation of

crystallographic slip-based FIPs typically stabilize after only a few fretting cycles. The analysis is therefore run for five fretting cycles in order to investigate predicted crack location and number of cycles to crack initiation.

Figure 18 shows the CPFE predicted distributions compared with Hertz [45] and Cattaneo-Mindlin [46],[47] elastic solutions for contact pressure and shear traction distributions, respectively. Both solutions show general agreement, although a number of peaks and troughs can be seen for the CPFE model resulting from the localised plasticity within the microstructure, as expected. The analytical solutions are based on the assumption of a homogeneous elastic material, and thus predict uniform distributions.
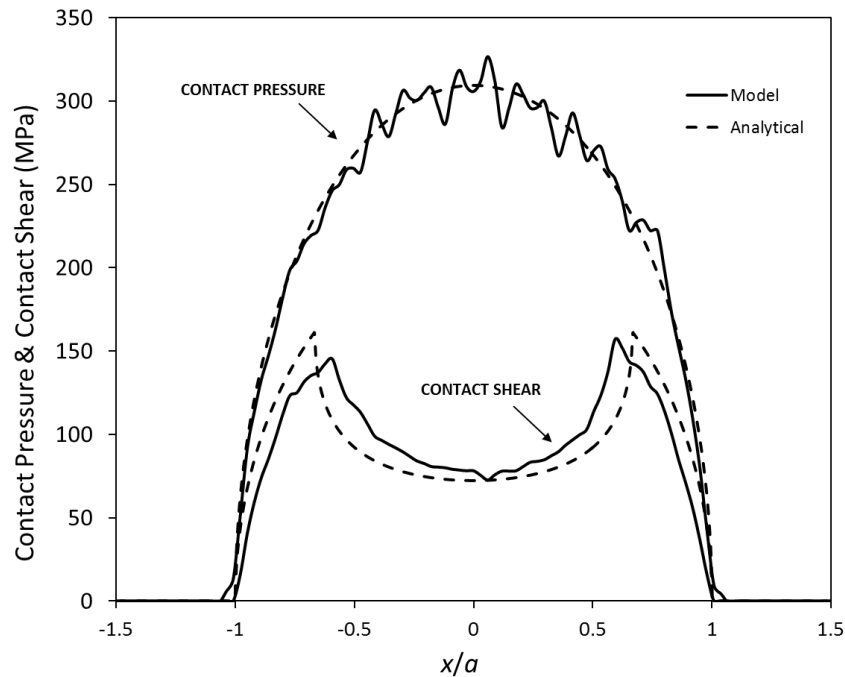

Figure 18. Comparison of CPFE-predicted and analytical distributions of contact pressure and shear traction across the contact.

4.2 FCI Location and Initial Orientation

Figure 19 shows the predicted distributions of p and P_{FS} after five fretting cycles, indicating the critical locations where crack initiation is predicted. As expected, plastic strain is concentrated in the micro-slip regions near the contact edges. The maximum FIP values are therefore predicted in these regions, as both parameters are based on the accumulation of crystallographic slip. These results are consistent with numerous experimental results available in the literature [6], where fretting cracks have been found to occur within the slip zone. This is in contrast to previously-used (continuum-based) FIPs which consistently predict cracking at or just outside the contact edge (trailing edge), as discussed earlier.
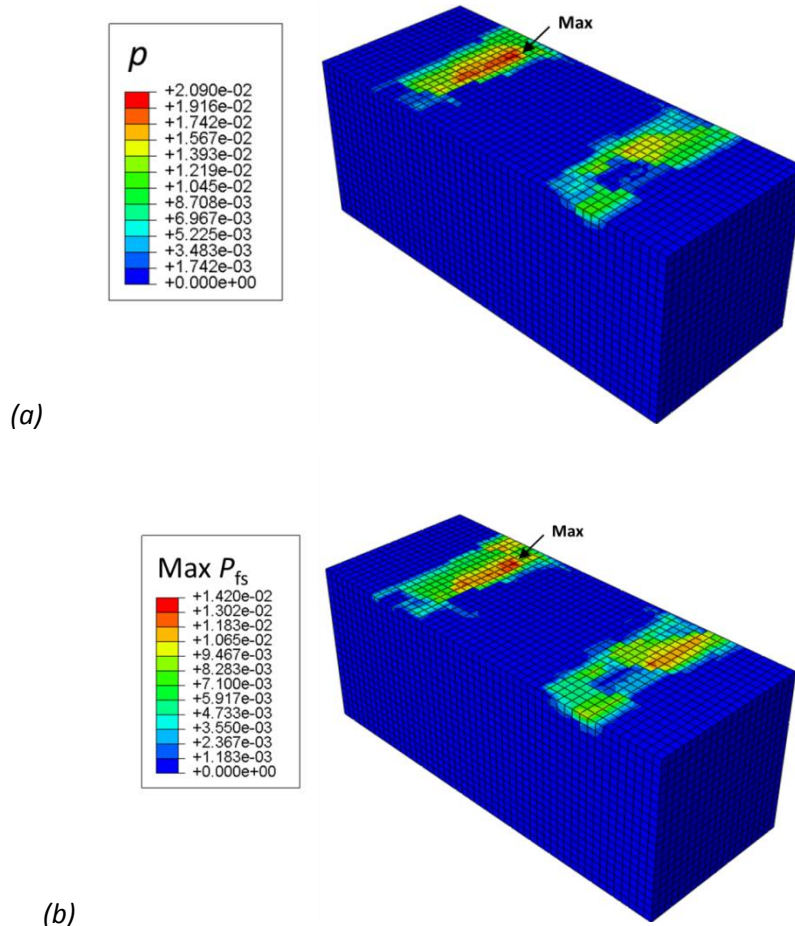
(a)

(b)

Figure 19. Contour plots of (a) p and (b) P$_{FS}$ in the substrate contact region (R = 6 mm) of the model after 5 fretting cycles.

Figure 19b shows two clear regions where high values of P_{FS} accumulate, corresponding to specific instances of microstructurally 'weak' grains, with respect to crack initiation, in micro-slip zones. These grains are highlighted in the microstructure shown in Fig. 20a. The P_{FS} parameter identifies critical crystallographic planes. The initial cracking direction is assumed to follow the critical crystallographic plane in each of these grains, that is, the crystallographic plane which accumulates the largest value of P_{FS}. These critical planes are highlighted in the BCC unit cell in Fig. 20b. Figure 18c illustrates the initial crack path based on this critical plane method, where one crack is predicted to grow at 52° to the surface towards the centre of contact and another is predicted to grow away from the contact at an angle of 84°. The 52° crack is considered to be dominated by crystallographic slip accumulation, and hence, grows at a shallow angle into the substrate. The normal stress contribution to P_{FS} is more significant for the 84° crack, as the critical plane is oriented near-perpendicular to the surface, and occurs closer to the edge of contact, where tangential stresses are more dominant. These results agree with a number of published observations regarding fretting fatigue crack location and initial orientation, e.g. [7],[9]. The microstructure-based P_{FS} parameter is therefore a useful method for predicting crack initiation.
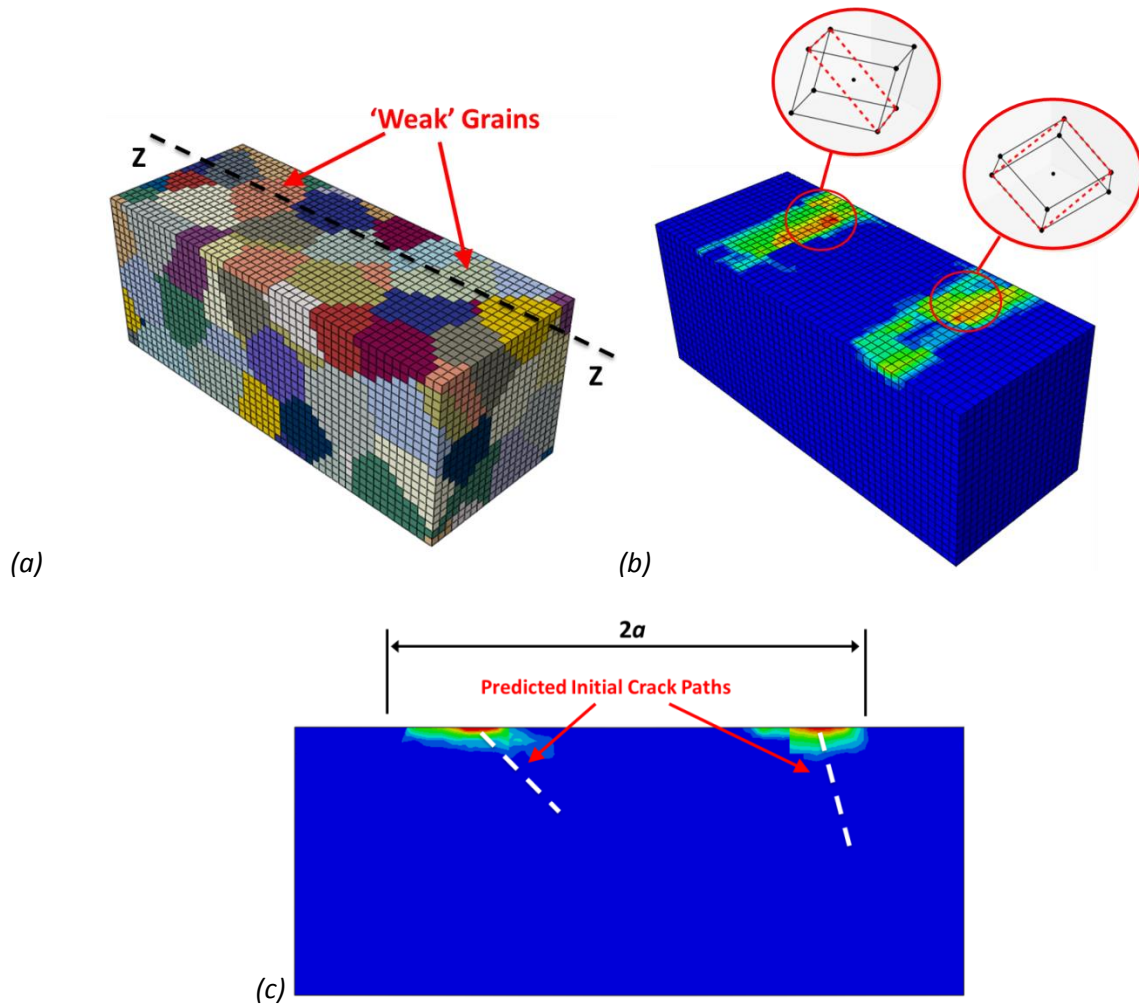
Figure 20. (a) The microstructure mesh, highlighting the two grains where cracking is most likely to occur, (b)the critical crystallographic plane of each grain, shown in dashed red lines and (c) a section view along the path ZZ, showing the predicted crack location and initial critical-place (path) direction relative to the surface.

4.3 Strain Gradient Effects

A key novelty of the current work is the implementation of a strain-gradient, crystal plasticity model for calculating GND density in fretting. The model is therefore capable of capturing the effects of localised hardening due to the high gradients of plastic strain, which potentially arise at the contact edges. The significance of this effect is quantified here by comparing the previously described model with a larger, equivalent scaled-up model. The scaled-up model is ten times larger (R = 60 mm, average d = 110 μm, a = 340 μm) with the identical nominal contact stresses (peak contact pressure and shear traction), identical microstructure geometry (except for absolute length) and identical a/d ratio (a/d = 3.1), viz. contact to (average) grain size ratio. This excludes statistical (microstructure) effects, as previously studied by the authors [12], allowing isolation of the length-scale effects of strain gradient. In other words, the same distribution of plastic strains will occur, but over different length-scales, thus giving different strain gradients in otherwise identical fretting conditions.

Figure 21 shows the predicted distributions of p and GND density after five cycles for both length-scale models. It is clear that regions of concentrated (high) p are more localised in the smaller length-scale, R = 6 mm, model. This is due to the relatively higher GND density in the micro-slip region, as shown in Fig. 21b, due to the fact that the slip region covers a smaller absolute length

scale but, with the same differential of plastic strain, it has a higher plastic strain gradient and hence higher GND density. The presence of these immobile GNDs result in slip system hardening, and thus, inhibit crystallographic slip. Conversely, the GND density in the micro-slip zones of the R = 60 mm model is negligible and insignificant GND hardening occurs. It is worth noting that when the strain gradient (GND) effects are omitted, both models show identical results.
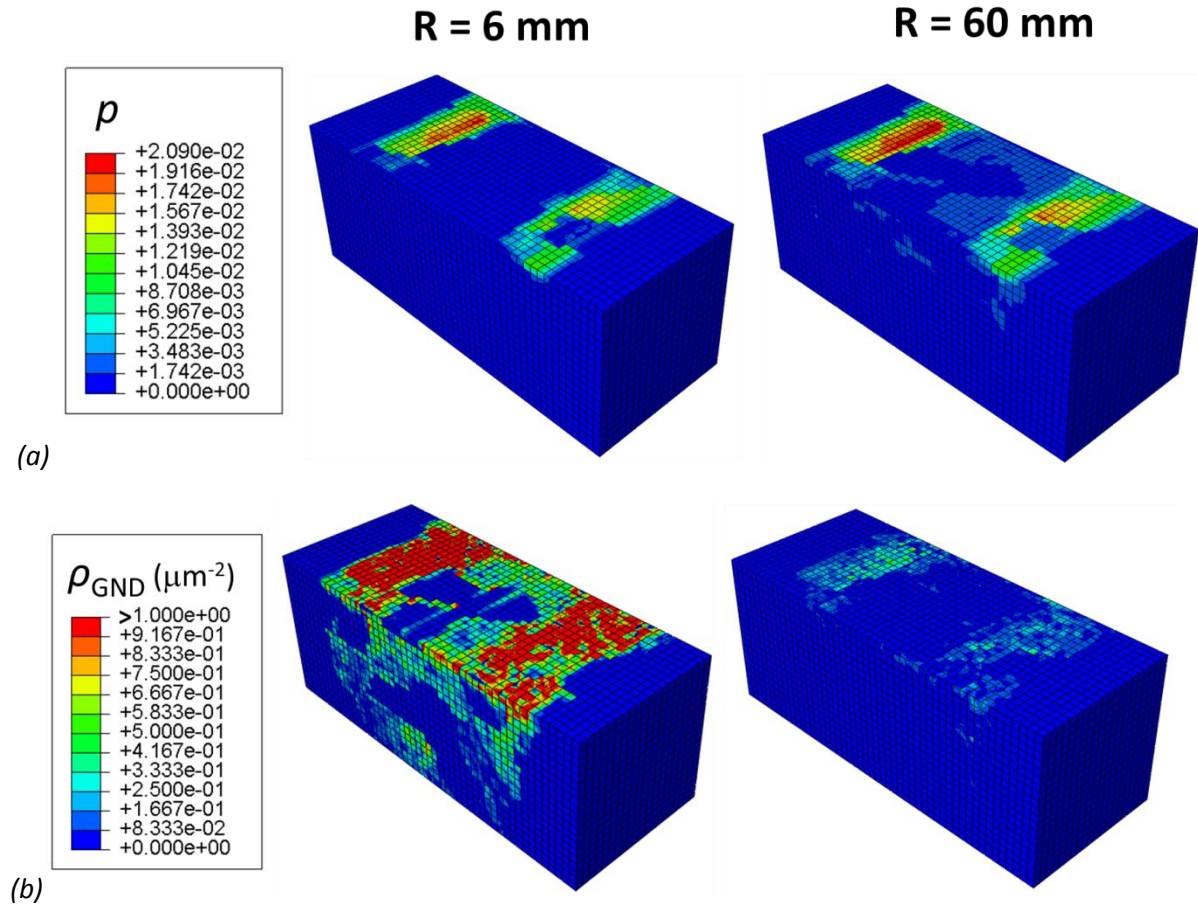

Figure 21. Contour plots of (a) accumulated plastic strain p and (b) GND density for a 6 mm cylinder radius model and a scaled-up 60 mm cylinder radius model.

In order to quantify this length-scale effect in fatigue, the cyclic accumulation of each FIP, p and P_{FS} is employed to predict number of cycles to crack initiation, following the methodology described in Section 3. Although the critical grain for crack initiation is the same for both models, the exact material point with maximum p and P_{FS} is different. This is a direct consequence of the strain gradient effects. Table 3 shows a comparison of the cyclic accumulation of p and P_{FS}, and corresponding predicted N_i values for the critical material point in each model over the first five fretting cycles. The predicted increase in N_i as the cylinder radius is reduced from 60 mm to 6 mm is also shown. It can be seen that the cyclic accumulation of each FIP is greater for the R = 60 mm model after each cycle, with the exception of cycle 3. The most significant effect is seen after the first cycle. It is clear that the cyclic accumulation of p and P_{FS} has not yet stabilised after five cycles. If the average cyclic accumulation is considered, it can be seen that the scaled-up R = 60 mm model is more susceptible to fatigue damage. Again, this can be explained by the presence of higher strain gradients in the smaller (R = 6 mm) model leading to higher densities of GNDs, which hinder accumulation of crystallographic slip, the primary variable for both FIPs. The considerably lower density of GNDs seen in the R = 60 mm geometry, as shown in Fig. 21b, results in more accumulated crystallographic slip, and therefore higher cyclic accumulation of p and P_{FS}.

Table 3.Cyclic accumulation of (a) p and (b) P_{FS} for R = 6 mm and R = 60 mm fretting models.

Cycle	p_{cyc}		N_i		$\dfrac{N_i^{6\,mm}}{N_i^{60\,mm}}$
	6 mm	60 mm	6 mm	60 mm	
1	0.0024	0.0034	304832	168058	1.81
2	0.0031	0.0039	194502	132271	1.47
3	0.0038	0.0036	138722	151931	0.91
4	0.0035	0.0041	158470	119691	1.32
5	0.0038	0.0039	134116	132958	1.01
Average	0.0033	0.0038	173038	139437	1.24

(a)

Cycle	P^{FS}_{cyc}		N_i		$\dfrac{N_i^{6\,mm}}{N_i^{60\,mm}}$
	6 mm	60 mm	6 mm	60 mm	
1	0.0016	0.0023	163910	100130	1.64
2	0.0021	0.0025	110023	88829	1.24
3	0.0028	0.0024	73760	94150	0.78
4	0.0023	0.0026	98038	83436	1.18
5	0.0027	0.0030	79646	68824	1.16
Average	0.0023	0.0025	98065	85858	1.14

(b)

5.0 Discussion

The present study has attempted to isolate the effect of strain-gradients in fretting, by removing statistical size effects (see [12]). This was achieved by maintaining a constant a/d ratio for the two fretting size-scales considered. The length-scale effects shown in the results of Table 3 are attributable to the combined effects of (i) contact slip-zone width, and (ii) grain size. The uniaxial fatigue results of Fig. 13 show the effect of grain size alone; the predicted effect on LCF life of reducing grain size by a factor of 10, from 400 μm to 40 μm, was ~10%. However, the cyclic loading in the partial slip fretting cases is multiaxial in nature and is due to slip-zone contact shear (friction), superimposed on an effectively constant contact pressure, giving mean stress-strain effects. As seen in Fig. 21b, the regions of high GND densities occur almost exclusively in the micro-slip region of the contact. The 6 mm case has therefore a significantly higher strain gradient effect. Table 3 shows the combined effects of slip-zone and grain size effects in fretting lead to between 14% and 24% average increase in life, for a factor of 10 (proportional) reduction in contact and grain size. This suggests an accentuating effect of fretting (cyclic) stresses on life of up to 14%. This observed trend suggests that the high strain gradients associated with small contact widths enhance fretting fatigue performance, consistent with the previously-published size effect in fretting [22],[23]. Future work aims to expand the present study to cover a broader range of microstructures, contact sizes and loading conditions, including more direct comparison with microstructure-sensitive experimental fretting results, to more comprehensively characterise the combined strain-gradient and statistical microstructural effects on fatigue crack initiation in fretting.

6.0 Conclusions

A framework has been developed to model the micromechanical behaviour of a dual-phase steel used in flexible marine risers. A length-scale dependent crystal plasticity model has been calibrated against experimental data in order to study crack initiation in fretting. Model predictions for crack initiation show agreement with experimental results.

A microstructure sensitive fretting model has shown that cracks can nucleate anywhere within the micro-slip zones of the contact. The implementation of a micro-scale Fatemi-Socie type parameter shows that cracks which nucleate near the contact edge initially grow near-normal to the surface of the substrate whereas cracks that nucleate within the slip zone, away from the contact edge, grow at acute angles. The present methodology captures stochastic effects due to random crystallographic orientation of metallic grains in the contact.

The role of strain-gradient effects has been quantified by comparing two equivalent fretting models with significantly contrasting characteristic length-scales. Small contact widths are shown to be more favourable in fretting fatigue due to increased slip system hardening as a consequence of higher density of geometrically necessary dislocations.

7.0 Acknowledgements

8.0 References

[1]   J. J. Madge, S. B. Leen, and P. H. Shipway, "A combined wear and crack nucleation-propagation methodology for fretting fatigue prediction," Int. J. Fatigue, vol. 30, no. 9, pp. 1509–1528, 2008.

[2]   J. Ding, D. Houghton, E. J. Williams, and S. B. Leen, "Simple parameters to predict effect of surface damage on fretting fatigue," Int. J. Fatigue, vol. 33, no. 3, pp. 332–342, 2011.

[3]   A. Fatemi and D. F. Socie, "A critical plane approach to multiaxial fatigue damage including out-of-phase loading," Fatigue Fract. Eng. Mater. Struct., vol. 11, no. 3, pp. 149–165, 1988.

[4]   T. T. K Smith, P Watson, "Stress-strain function for the fatigue of metals," J. Mater., vol. 5, pp. 767–778, 1970.

[5]   C. Ruiz, P. H. B. Boddington, and K. C. Chen, "An investigation of fatigue and fretting in a dovetail joint," Exp. Mech., vol. 24, no. 3, pp. 208–217, Sep. 1984.

[6]   J. A. Araújo and D. Nowell, "The effect of rapidly varying contact stress fields on fretting fatigue," Int. J. Fatigue, vol. 24, no. 7, pp. 763–775, 2002.

[7]   V. Lamacq, M.-C. Dubourg, and L. Vincent, "A theoretical model for the prediction of initial growth angles and sites of fretting fatigue cracks," Tribol. Int., vol. 30, no. 6, pp. 391–400, 1997.

[8]   J. A. Araújo, G. M. J. Almeida, J. L. A. Ferreira, C. R. M. da Silva, and F. C. Castro, "Early cracking orientation under high stress gradients: The fretting case," Int. J. Fatigue, vol. 100, pp. 611–618, 2017.

[9]   C. Navarro, J. Vázquez, and J. Domínguez, "Nucleation and early crack path in fretting fatigue," Int. J. Fatigue, vol. 100, pp. 602–610, 2017.

[10]   O. J. McCarthy, J. P. McGarry, and S. B. Leen, "The effect of grain orientation on fretting fatigue plasticity and life prediction," Tribol. Int., vol. 76, pp. 100–115, 2013.

[11]   T. Dick and G. Cailletaud, "Fretting modelling with a crystal plasticity model of Ti6Al4V," Comput. Mater. Sci., vol. 38, no. 1, pp. 113–125, 2006.

[12]   P. J. Ashton, A. M. Harte, and S. B. Leen, "Statistical grain size effects in fretting crack initiation," Tribol. Int., vol. 108, no. September 2016, pp. 75–86, 2016.

[13]   M. Zhang, R. W. Neu, and D. L. McDowell, "Microstructure-sensitive modeling: Application to fretting contacts," Int. J. Fatigue, vol. 31, no. 8–9, pp. 1397–1406, 2009.

[14]   F. P. E. Dunne. A. Manonukul, "High- and low- cycle fatigue crack initiation using polycrystal plasticity," Proc. R. Soc. A Math. Phys. Eng. Sci., vol. 460, pp. 1881–1903, 2004.

[15]   M. F. Ashby, "The deformation of plastically non-homogeneous materials," Philos. Mag., vol. 21, no. 170, pp. 399–424, 1970.

[16]   H. Gao and Y. Huang, "Geometrically necessary dislocation and size-dependent plasticity," Scr. Mater., vol. 48, no. 2, pp. 113–118, 2003.

[17]   N. A. Fleck, G. M. Muller, M. F. Ashby, and J. W. Hutchinson, "Strain gradient plasticity: Theory and experiment," Acta Metall. Mater., vol. 42, no. 2, pp. 475–487, 1994.

[18]   C. A. Sweeney, B. O'Brien, F. P. E. Dunne, P. E. McHugh, and S. B. Leen, "Strain-gradient modelling of grain size effects on fatigue of CoCr alloy," Acta Mater., vol. 78, pp. 341–353, Oct. 2014.

[19]   E. P. Busso, F. T. Meissonnier, and N. P. O'Dowd, "Gradient-dependent deformation of two-phase single crystals," J. Mech. Phys. Solids, vol. 48, no. 11, pp. 2333–2361, 2000.

[20]   C. F. Niordson and B. N. Legarth, "Strain gradient effects on cyclic plasticity," J. Mech. Phys. Solids, vol. 58, no. 4, pp. 542–557, 2010.

[21]   D. Liu, Y. He, L. Shen, J. Lei, S. Guo, and K. Peng, "Accounting for the recoverable plasticity and size effect in the cyclic torsion of thin metallic wires using strain gradient plasticity," Mater. Sci. Eng. A, vol. 647, pp. 84–90, 2015.

[22]   J. A. Araújo and D. Nowell, "Analysis of pad size effects in fretting fatigue using short crack arrest methodologies," Int. J. Fatigue, vol. 21, no. 9, pp. 947–956, 1999.

[23]   R. Bramhall, "Studies in fretting fatigue," University of Oxford, 1973.

[24]   Sinead O'Halloran, "Experimental characterisation, computational modelling and design tool development for fretting fatigue and wear in flexible marine risers," NUI Galway, 2017.

[25]   V. S. Sarma and K. A Padmanabhan, "Low cycle fatigue behaviour of a medium carbon microalloyed steel," Int. J. Fatigue, vol. 19, no. 2, pp. 135–140, 1997.

[26]   S. Sankaran, V. S. Sarma, and K. A Padmanabhan, "Low cycle fatigue behavior of a multiphase microalloyed medium carbon steel : comparison between ferrite pearlite and quenched and tempered microstructures," Mater. Sci. Eng. A, vol. 345, pp. 328–335, 2003.

[27]   D. L. McDowell and F. P. E. Dunne, "Microstructure-sensitive computational modeling of fatigue crack formation," Int. J. Fatigue, vol. 32, no. 9, pp. 1521–1542, 2010.

[28]   F. P. E. Dunne, R. Kiwanuka, and A. J. Wilkinson, "Crystal plasticity analysis of micro-deformation, lattice rotation and geometrically necessary dislocation density," Proc. R. Soc. A Math. Phys. Eng. Sci., vol. 468, no. 2145, pp. 2509–2531, 2012.

[29]   F. P. E. Dunne, D. Rugg, and A. Walker, "Lengthscale-dependent, elastically anisotropic, physically-based hcp crystal plasticity: Application to cold-dwell fatigue in Ti alloys," Int. J. Plast., vol. 23, no. 6, pp. 1061–1083, 2007.

[30]   G. B. Gibbs, "Thermodynamic analysis of dislocation glide controlled by dispersed local obstacles," Mater. Sci. Eng., vol. 4, no. 6, pp. 313–328, Sep. 1969.

[31]   G. I. Taylor, "The Mechanism of Plastic Deformation of Crystals. Part I. Theoretical," Proc. R. Soc. A Math. Phys. Eng. Sci., vol. 145, pp. 3625–387, 1934.

[32]   A. Ma, F. Roters, and D. Raabe, "A dislocation density based constitutive model for crystal plasticity FEM including geometrically necessary dislocations," Acta Mater., vol. 54, no. 8, pp. 2169–2179, 2006.

[33]   J. F. Nye, "Some geometrical relations in dislocated crystals," Acta Mater., no. 1, pp. 153–162, 1953.

[34]   A. Arsenlis and D. M. Parks, "Crystallographic aspects of geometrically-necessary and statistically-stored dislocation density," Acta Mater., vol. 47, no. 5, pp. 1597–1611, 1999.

[35]   R. Kiwanuka, "Micro-deformation and Texture in Engineering Materials," University of Oxford, 2013.

[36]   P. J. Ashton, T. S. Jun, Z. Zhang, T. B. Britton, A. M. Harte, S. B. Leen, and F. P. E. Dunne, "The effect of the beta phase on the micromechanical response of dual-phase titanium alloys," Int. J. Fatigue, vol. 100, pp. 377–387, 2017.

[37]   N. Ishikawa, D. M. Parks, S. Socrate, and M. Kurihara, "Micromechanical modeling of ferrite-pearlite steels using finite element unit cell models," ISIJ Int., vol. 40, no. 11, pp. 1170–1179, 2000.

[38]   P. Kucharczyk, M. Sharaf, and S. Münstermann, "On the influence of steel microstructure on short crack growth under cyclic loading," Int. J. Fatigue, vol. 41, pp. 83–89, 2012.

[39]   C. J. Bayley, W. a M. Brekelmans, and M. G. D. Geers, "A comparison of dislocation induced back stress formulations in strain gradient crystal plasticity," Int. J. Solids Struct., vol. 43, no. 24, pp. 7268–7286, 2006.

[40]   P. Franciosi, L. T. Le, G. Monnet, C. Kahloun, and M. H. Chavanne, "Investigation of slip system activity in iron at room temperature by SEM and AFM in-situ tensile and compression tests of iron single crystals," Int. J. Plast., vol. 65, pp. 226–249, 2015.

[41]   C. A. Sweeney, W. Vorster, S. B. Leen, E. Sakurada, P. E. McHugh, and F. P. E. Dunne, "The role of elastic anisotropy, length scale and crystallographic slip in fatigue crack nucleation," J. Mech. Phys. Solids, vol. 61, no. 5, pp. 1224–1240, 2013.

[42]   A. Cruzado, S. Lucarini, J. LLorca, and J. Segurado, "Microstructure-based fatigue life model of metallic alloys with bilinear Coffin-Manson behavior," pp. 1–25, 2017.

[43]   M. Sharaf, P. Kucharczyk, N. Vajragupta, S. Münstermann, A. Hartmaier, and W. Bleck, "Modeling the microstructure influence on fatigue life variability in structural steels," Comput. Mater. Sci., vol. 94, no. C, pp. 258–272, 2014.

[44]   K. S. Chan, "A Microstructure-Based Fatigue-Crack-Initiation Model," Met. Mat. Trans. A, vol. 34, pp. 43–57, 2003.

[45]   H. Hertz, "Über die Berührung fester elastischer Körper," J. fur die Reine und Angew. Math., pp. 156–171, 1882.

[46]   C. Cattaneo, "Sul contatto di due corpi elastici: distribuzione locale degli sforzi," Rend. Accad. Naz., vol. Lincei 27, pp. 342–348, 1938

[47]   R. D. Mindlin, "Compliance of elastic bodies in contact," J. Appl. Mech., vol. 16, pp. 259–268, 1949.